J Nanopart Res (2015) 17:86
DOI 10.1007/s11051-015-2894-8

RESEARCH PAPER

Ag nanoparticles formed by femtosecond pulse laser ablation in water: self-assembled fractal structures

Jesica M. J. Santillán · Marcela B. Fernández van Raap · Pedro Mendoza Zélis · Diego Coral · Diego Muraca · Daniel C. Schinca · Lucía B. Scaffardi

Received: 22 September 2014 / Accepted: 28 January 2015

Abstract We report for the first time on the formation of self-assembled fractals of spherical Ag nanoparticles (Nps) fabricated by femtosecond pulse laser ablation of a solid silver target in water. Fractal structures grew both in two and three Euclidean dimensions (d). Ramified-fractal assemblies of 2 nm height and 5–14 μm large, decorated with Ag Nps of 3 nm size, were obtained in a $2d$ geometry when highly diluted drops of colloidal suspension were dried at a fast heating rate over a mica substrate. When less-diluted drops were dried at slow heating rate, isolated single Nps or rosette-like structures were formed. Fractal aggregates about 31 nm size in $3d$ geometry were observed in the as-prepared colloidal suspension. Electron diffraction and optical extinction spectroscopy (OES) analyses performed on the samples confirmed the presence of Ag and Ag_2O. The analysis of the optical extinction spectrum, using the electrostatic approximation of Mie theory for small spheres, showed the existence of Ag bare core, Ag–Ag_2O and air–Ag core–shell Nps, Ag–Ag_2O being the most frequent type [69 % relative abundance (r.a.)]. Core-size and shell-thickness distribution was derived from OES. In situ scattering measurements of the Ag colloidal suspension, carried out by small-angle X-ray scattering, indicate a mass fractal composed of packaged $\langle D_{\mathrm{SAXS}}\rangle = (5 \pm 1)$ nm particles and fractal dimension $d_f = 2.5$. Ex situ atomic force microscopy imaging displayed well-ramified structures, which, analyzed with box-counting method, yield a fractal dimension $d_f = 1.67$. The growing behavior of these $2d$ and $3d$ self-assembled fractals is consistent with the diffusion-limited aggregation model.

Keywords Fractal · Silver nanoparticles · fs laser ablation · SAXS · AFM

J. M. J. Santillán · D. C. Schinca · L. B. Scaffardi (✉)
Centro de Investigaciones Ópticas (CIOp), CONICET La Plata-CIC, La Plata, Argentina
e-mail: lucias@ciop.unlp.edu.ar

M. B. Fernández van Raap · P. Mendoza Zélis · D. Coral
Instituto de Física La Plata (IFLP), CONICET, La Plata, Argentina

M. B. Fernández van Raap (✉) · P. Mendoza Zélis · D. Coral
Departamento de Física, Facultad de Ciencias Exactas, UNLP, La Plata, Argentina
e-mail: raap@fisica.unlp.edu.ar

P. Mendoza Zélis · D. C. Schinca · L. B. Scaffardi
Departamento de Ciencias Básicas, Facultad de Ingeniería, UNLP, La Plata, Argentina

D. Muraca
Instituto de Física "Gleb Wataghin" (IFGW), Universidade Estadual de Campinas, Campinas, Brazil

Introduction

Silver nanoparticles (Nps) have received considerable attention among noble metal nanomaterials due to their attractive physicochemical properties, which boosted applications in catalysis, optics, electronics,

Published online: 08 February 2015

and other areas based on their unique size-dependent optical and electrical properties. The surface plasmon resonance and the large effective scattering cross section of individual silver Nps make them ideal candidates for molecular labeling (Schultz et al. 2000).

There are basically two approaches to the generation of Nps: bottom-up and top-down methods. In the former, the nanomaterial is formed through atom-to-atom attachment via a wet chemical reaction or via vapor phase deposition. In the latter approach, energy is deposited in a bulk material at a sufficient fast rate so that it breaks up and forms structures in the nanometric scale (Siekmann et al. 1991; Baker et al. 2000; Bewig et al. 1992; Ishii et al. 1999). Within this approach, laser ablation has many interesting characteristics. First, it has a high deposition rate as compared to other methods such as electron beam deposition, magnetron sputtering, and chemical vapor deposition. Second, it is a non-contaminating source of energy transfer (green technique), such that the colloidal suspensions are free from unwanted products. Third, pulsed laser ablation process can be applied to a wide variety of materials and in a wide range of environments. In the last years, ultrashort pulse lasers were particularly used for ablation of solid targets in liquids, obtaining spherical metal Nps colloids (Kabashin and Meunier 2006; Santillán et al. 2012, 2013a–c; Barcikowski et al. 2007) with sizes ranging from a few tens of nm down to 1 nm.

In spite of the different experimental conditions encountered in both methodologies, formation of complex assemblies of individual Nps has been observed. Yan et al. (2013) reported the generation of Ag–Ag_2O complex nanostructures after excimer laser ablation (30 ns, $\lambda = 248$ nm) of an Ag solid target in water. Zenkevich et al. (2002) report the formation of fractal gold clusters of approximately 5 nm primary particle diameter, deposited on highly ordered pyrolytic graphite with 10 ns Nd:YAG laser by pulsed laser deposition (PLD) technique. The authors suggested that the shape and dimension of the clusters are determined by the rate at which Au atoms arrive at the surface where the formation occurs, influenced by the surface symmetry. It was proposed that the formation of clusters proceeds under highly nonequilibrium conditions by the attachment of an adatom to the fractal nucleus. Qu and Dai (2005) reported hierarchical ramified-like silver nanostructures prepared by carrying out the silver mirror reaction on copper foils. Dong et al. (2012) obtained Ag fractal-like nanostructures decorated with Ag Nps using electrochemical deposition on a plastic surface. These ramified-like nanostructured materials have attracted great attention due to their unique properties leading to possible applications in catalysis and technological areas such as glucose and hydrogen peroxide sensors (Liu and Wang 2013; Zhou et al. 1999; Qiu et al. 2007, 2009; Sun and Hagner 2007). The presence of abundant edges and ridges in ramified silver nanostructures enables having a lot of active atoms that can be used for single-molecule detection through surface-enhanced Raman scattering (Wen et al. 2006; Wang et al. 2008).

We report for the first time the observation of fractal structuring in an Ag colloid produced by femtosecond pulse laser ablation in water. Dispersed phase $3d$ fractal structuring and size distribution was in situ observed in the as-prepared suspension by small-angle X-ray scattering (SAXS). Atomic force microscopy (AFM) imaging was ex situ used to study $2d$ fractal structuring and also used to analyze the shape and size of isolated Nps after drying a drop of diluted colloidal suspension on a muscovite mica substrate at different initial heating rates. Transmission electron microscopy (TEM) and optical extinction spectroscopy (OES) were also used to study the size distribution of individual Nps, its shape, and structure. Electron diffraction was used for phase identification. Finally, the growing behavior of these $2d$ and $3d$ self-assembled fractals is discussed in terms of the diffusion-limited aggregation (DLA) model.

Although fractal structures are often found in nature and have been widely studied from experimental, theoretical, and simulation points of view i.e., images are often created using fractal generating codes (Singh et al. 2011; Hou et al. 1998; Parfenov et al. 2003; Qiu et al. 2007; Ding et al. 2010; Shelke et al. 2013), the experimental conditions under which a specific structuring for a given colloid can be obtained, is still an open question. The knowledge of these conditions could help defining control parameters for nanostructured material design.

Experimental

Colloidal silver Nps were fabricated by ultrafast pulse laser ablation. The target sample used to carry out

these experiments was a 1-mm-thick circular disk of high-purity grade silver immersed in 1 cm depth in vessel filled with 4 ml of milli-Q water. Laser ablation was performed using a Ti:sapphire chirped-pulsed amplification system from Spectra Physics, emitting pulses of 100 fs width at 1 kHz repetition rate centered at 800 nm wavelength. The maximum output energy was 1 mJ/pulse, but it could be attenuated using a classical waveplate–polarizer system. A 5 cm focal length lens was used to focus the laser beam on the target disk surface. The pulse energy used in this experiment was 500 μJ. Considering the focal length of the focusing lens and the input beam diameter, the used fluence was 450 J/cm^2. The sample was moved using a XY motorized micrometric stage. The movement was programed so that the laser impinged always in different points of the sample. In this way, ablation was performed always from a fresh surface of the sample. This process lasted 9 min, after which the large number of Nps generated in the suspension produced a typical yellowish color in water. The concentration of the as-prepared colloidal suspension was 1.6×10^{-5} M, as determined from the extinction spectrum using Lambert–Beer law.

To generate $2d$ fractal structure, part of the as-prepared colloidal suspension was sonicated and diluted to 1/50 and 1/100 (v/v) in milli-Q water. A drop of such diluted sample was placed on a freshly cleaved muscovite mica sheet V-1 grade (SPI Supplies) at room temperature (25 °C) and then dried in an oven at atmospheric pressure. To enhance the possible development of fractal-like structures, the drop was dried increasing the temperature from 25 to 36 °C or from 25 to 50 °C, in a time interval of 15 min. In this way, the drop was exposed to an initial temperature difference of 9 and 25 °C, respectively, establishing distinct initial heating rates.

The observation of $2d$ fractal structures was carried out with AFM (NT-MDT Solver Pro) microscope equipped with an Appnano-Acta silicon probe consistent for high resolution imaging. AFM images were recorded in air at room temperature using the standard semicontact mode. The rectangular cantilever of 40 N/m force constant and 281.8 kHz resonant frequency holds a sharp tip of 6-nm curvature radius. The minimum scanning step in vertical direction (z) is 0.012 nm and defines the z resolution. The analysis of mica sheet AFM measurement indicates an average roughness of 0.0612 nm. These facts make the AFM an adequate technique to observe nanometric and subnanometric particles and their self-assembled nanostructures.

Microscopy images and electron diffraction were preformed with a TEM-MSC (JEOL 2100) at Brazilian Synchrotron Light Laboratory (LNLS). The as-prepared Ag aqueous suspensions were diluted in milli-Q water and sonicated during 15 min. Samples were obtained by drying the water-dispersed Nps on a carbon-coated copper grids. Images were acquired with the sample on a single-tilt sample holder and a TV Gatan ES500W and CCD (TVips-16MP) cameras.

SAXS data were collected at D2S-SAXS2 beam line of LNLS using Mars 165 CCD-detector at a wavelength of $\lambda = 1.822$ Å ($\varepsilon = 6.804$ keV). For measurement, the as-prepared colloids were sonicated and injected in between the two clear ruby mica discs (25-μm thick each) of the liquid sample holder. The range of the momentum transfer vector $q = 4\pi\sin(\theta)/\lambda$ (being 2θ the scattering angle), spanned from 0.06 to 3 nm^{-1} and it was covered using two sample-detector distances. Water was used as a secondary standard to express scattering intensity in an absolute scale as differential cross section $\partial\Sigma/\partial\Omega$ (cm^{-1}) and to merge data from the two measurements. The raw data were corrected for absorption, background, and solvent density fluctuation scattering prior to fitting.

OES was conducted by means of a commercial Shimadzu spectrophotometer from 300 to 1,000 nm and it was performed on colloidal suspension immediately after fabrication.

Results

TEM analysis

A highly diluted colloidal suspension was prepared to avoid agglomeration effects. For this reason, many TEM images of few isolated Nps were acquired instead of panoramic-like views. Selected TEM images of a colloidal Ag Nps suspension generated by fs laser ablation in water are shown in Fig. 1. Several Nps structures (bare core or core–shell) and types (metal oxide and hollow Np) were observed. Panel (a) shows spherical Ag bare core Nps with Bragg interplanar separation of 0.23 nm, consistent with Ag crystalline structure. Core–shell structures

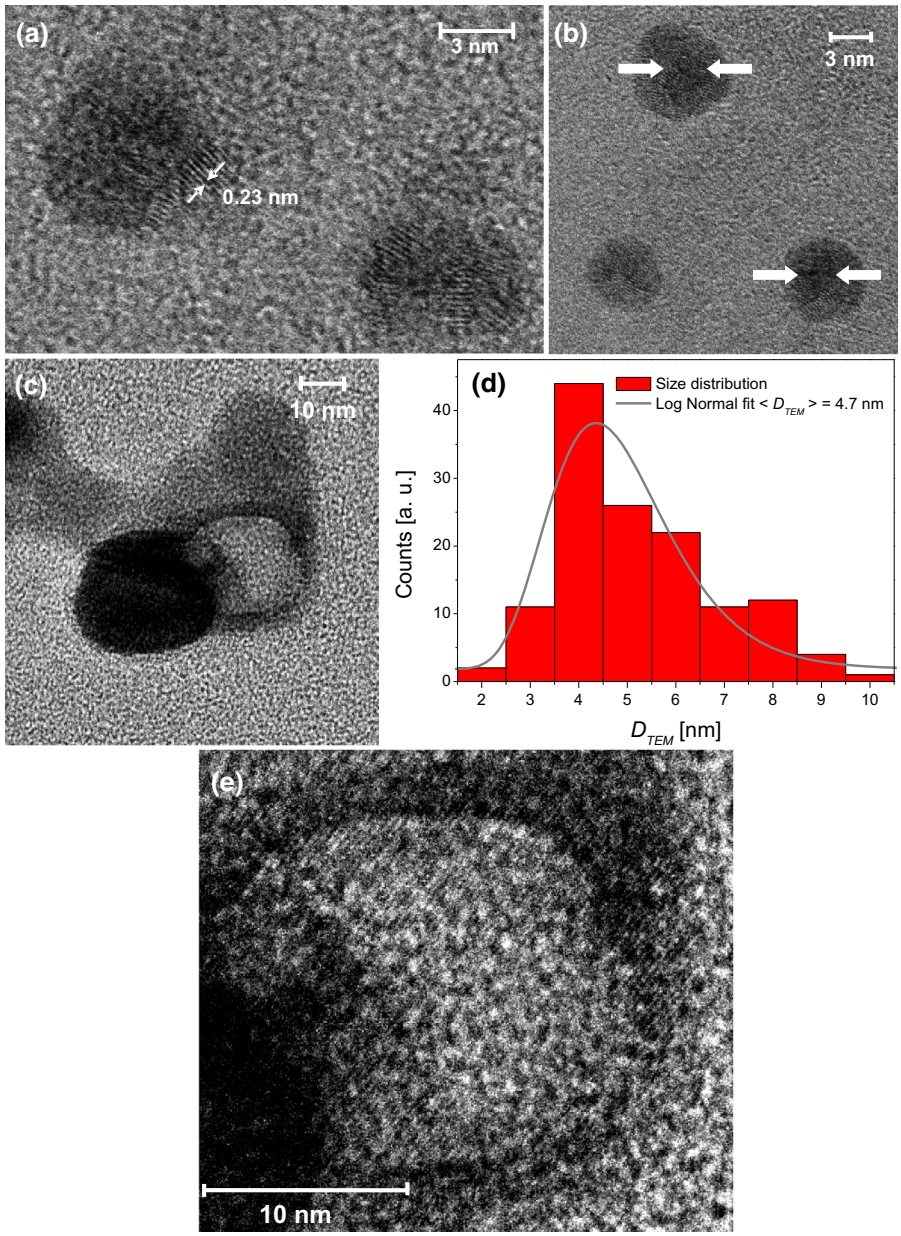

Fig. 1 TEM images of Nps present in the colloidal suspension generated by femtosecond laser ablation: **a** isolated silver bare core Nps, **b** isolated silver core–shell Nps, **c** hollow metal Np together with a bare core Np, **d** size histogram obtained by measuring 140 particles within the sample and log-normal fit curve and **e** enlargement of panel **c** where Bragg planes in the *central zone* of the hollow Np can be seen

can be resolved on TEM images based on the difference in contrast, which is proportional to atomic number *Z*. In this way, isolated silver core–shell Nps with 3 nm core size and about 1.5 nm silver oxide shell were also observed in several TEM micrographs, as shown in panel (b), while panel (c) shows a hollow metal Np together with a bare core Np. Panel (d) shows a size histogram obtained by measuring 140 particles within the sample. The histogram was fitted by a log-normal distribution with a mean size $\langle D_{\mathrm{TEM}} \rangle = 4.7$ nm and a half width of 1.8 nm. Panel (e) is an enlargement of panel (c) which shows Bragg planes in the central zone of the hollow Np, indicating that it is a spherical metal shell.

Electron diffraction

Electron diffraction patterns were carried out on selected Nps for phase identification. For quantitative analysis, the diffraction image of silver Nps from a dried colloidal suspension (inset of Fig. 2) was transformed into a plot of intensity diffraction profile versus electron wave vector q_e by azimuthal-intensity integration. The background of the diffraction profile was subtracted through a fitting procedure. In the so-obtained profile (Fig. 2), reflection line positions are more precisely determined. This pattern is indexed with the reflection lines of Ag (cubic, $Fm\bar{3}m$) and the most intense line of Ag_2O (cubic, $Pn\bar{3}m$) according to JCPDS #87-0720 and #75-1532, respectively. Reflection lines in Fig. 2 are labeled with Miller indices (h, k, l). No reflection characteristic of other silver oxide appears. Ag_2O is expected to appear from Ag oxidation because it is the only Ag oxide displaying cubic structure.

The reflection line positions were used to determine the lattice constant a using Bragg's law for cubic crystals: $q_{e_{hkl}} = \frac{2\pi(h^2+k^2+l^2)^{1/2}}{a}$. The so-obtained lattice constant for Ag is $a = (4.15 \pm 0.03)$ Å.

Electron diffraction pattern indicates only the presence of Ag and Ag_2O phases. Although it may be argued that the presence of silver oxide in the sample may come from oxidation during drying process, the inclusion of Ag–Ag_2O Nps to fit the extinction spectrum of silver Nps suspension evidences the formation of oxide shell during laser ablation synthesis.

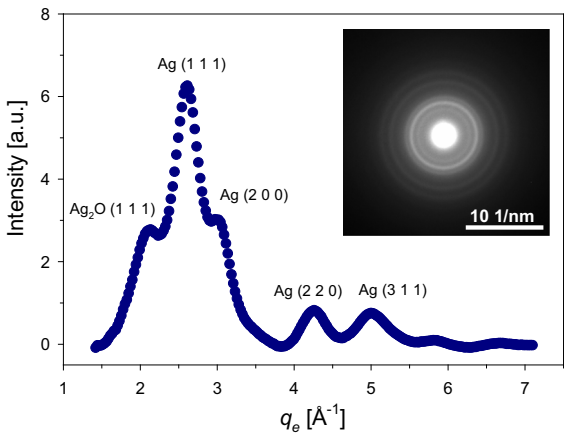

Fig. 2 Intensity profile against electron wave vector q_e of silver core–shell Nps obtained from an azimuthal integration of the electron diffraction pattern of the raw data shown in the *inset*

OES

OES was used to determine Nps size distribution and morphology (bare core and core–shell) along with its species in the as-prepared colloidal suspension. The response of optical extinction for small Nps compared with wavelength can be described using the electrostatic approximation of Mie theory. In this approach, the expression for the extinction cross section can be written as (Bohren and Huffman 1998):

$$C_{\text{ext}} = k' \text{Im}(\alpha), \tag{1}$$

where α is the polarizability, $k' = 2\pi n_m/\lambda$ is the wavenumber in the medium surrounding the particle, n_m is the refractive index of the medium, and λ is the wavelength of the incident light in vacuum.

For the general case of a spherical metal core–dielectric shell structure (Fig. 3), the polarizability α can be expressed as

$$\alpha = 4\pi R'^3 \frac{(\varepsilon_2 - \varepsilon_m)(\varepsilon_1 + 2\varepsilon_2) + f(\varepsilon_1 - \varepsilon_2)(\varepsilon_m + 2\varepsilon_2)}{(\varepsilon_2 + 2\varepsilon_m)(\varepsilon_1 + 2\varepsilon_2) + f(2\varepsilon_2 - 2\varepsilon_m)(\varepsilon_1 - \varepsilon_2)}. \tag{2}$$

Equation (2) contains the factor $f = (R/R')^3$ for the ratio between inner and outer radii volumes, with R being the radius of the central core and R' the outer radius (core + shell thickness). ε_1, ε_2 and ε_m are the dielectric functions of the core, shell, and surrounding medium, respectively. A parameter related to the extinction cross section which is often used for extinction spectra plotting purposes is the extinction coefficient defined as $Q_{\text{ext}} = C_{\text{ext}}/\pi R'^2$. The expression for the complex metal dielectric function in terms of λ and R was determined taking into account the

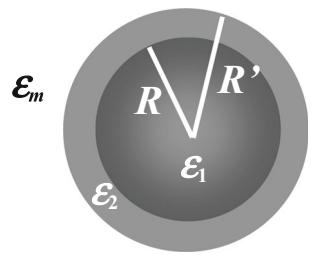

Fig. 3 Schematic of metal core–dielectric shell structure. R and R' are inner and outer radii, respectively

corrections for free and bound electron contributions as described in previous works (Scaffardi et al. 2013; Santillán 2013; Santillán et al. 2013a–c):

$$\varepsilon_{\text{size}}(\omega, R) = 1 - \frac{\omega_p^2}{\omega^2 + i\gamma_{\text{size}}(R)\omega} + K_{\text{size}}(R) \int_{\omega_g}^{\infty} \frac{\sqrt{x - \omega_g}}{x}[1 - F(x, T)] \frac{(x^2 - \omega^2 + \gamma_b^2 + i2\omega\gamma_b)}{(x^2 - \omega^2 + \gamma_b^2)^2 + 4\omega^2\gamma_b^2} dx, \quad (3)$$

where $\gamma_{\text{size}}(R) = \gamma_{\text{bulk}} + C(v_F/R)$ and $K_{\text{size}}(R) = K_{\text{bulk}}(1 - \exp(-R/R_0))$ are the size-corrected expressions for the free electron damping constant and the bound electron contribution coefficient. C is a constant related to electron scattering processes within the particles, as derived from first-principles calculations, whose value ranges from 0.6 to 1.2 depending on the metal. For silver, $C = 0.8$ was used (Kreibig and Vollmer 1995; Santillán et al. 2013a–c).

These calculations involve several physical magnitudes such as bulk plasma frequency ω_p, bulk damping constant γ_{bulk}, Fermi velocity v_F, gap energy E_g, Fermi energy E_F, damping constant for interband transitions γ_b, bound electron contribution coefficient K_{bulk}, and R_0 a scale factor. For silver, the values of these magnitudes are $\omega_p = 13.8 \times 10^{15}$ Hz (Johnson and Christy 1972), $\gamma_{\text{bulk}} = 2.7 \times 10^{13}$ Hz (Johnson and Christy 1972), $v_F = 14.1 \times 10^{14}$ nm/s (Kittel 2007), $K_{\text{bulk}} = 2 \times 10^{24}$ (Santillán et al. 2013a–c), $E_g = 1.91$ eV (Santillán et al. 2013a–c), $E_F = 4.12$ - eV (Santillán et al. 2013a–c), $R_0 = 0.35$ nm, and $\gamma_b = 1.5 \times 10^{14}$ Hz (Santillán et al. 2013a–c).

Figure 4 shows the normalized experimental extinction spectrum corresponding to the colloidal suspension together with the best theoretical fit using Eqs. (1)–(3). Silver dielectric function was taken from Johnson and Christy (1972) and dielectric function of Ag_2O from Qiu et al. (2005).

Fit of the extinction spectrum requires considering Ag bare core, Ag–Ag_2O, and air–Ag core–shell Nps in accordance with the structures and types shown by TEM and electron diffraction. It can be readily seen that considering only the first two kind of Nps, the theoretical extinction calculation (short dashed line curve) misses to fit the experimental curve for wavelengths

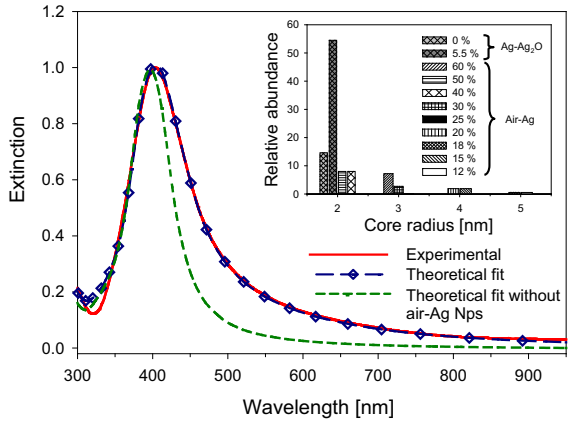

Fig. 4 Experimental optical extinction spectrum (*full line*) of silver colloidal suspension. Best theoretical fit (*long dashed-diamonds line*) was obtained for size distribution of core radii and shell thickness using Ag–Ag_2O, air–Ag and bare core Ag Nps, with r.a.s shown in the *inset*. *Bars* grouped around each integer core radius represent shell thickness distributions, structures (bare core or core–shell) and types (Ag, Ag–Ag_2O, and air–Ag). *Short dashed line* curve represents the theoretical simulation without considering air–Ag Nps

$\lambda > 397$ nm as well as its full width a half maximum (FWHM). Considering hollow Nps as well improves the fit of the spectrum (long dashed-diamonds line).

The inset in Fig. 4 shows the r.a. as a function of core radius for different shell thicknesses, structures, and types. The bars in the histogram corresponding to these three characteristics are grouped around integer core radius values used for the best fit. It must be stressed here that this distribution histogram is the result of an iterative process that changes sequentially different parameters such as core radii, shell thickness, and core–shell type. Each parameter modifies an independent feature of the spectra (plasmon peak, FWHM, and slope at long and short wavelengths), so the optimum physical parameters are unique in the sense that there is no other set of values that correctly fit the full spectrum.

Optimum distribution has a predominant core radius of 2 nm ($D_{\text{OES}} = 4$ nm), presenting a contribution of Ag bare core (14.6 % r.a.), Ag–Ag_2O (54.5 % r.a.) with 2.75 % D_{OES} shell thickness and air–Ag with 20 % D_{OES} shell thickness (8 % r.a.) and 25 % D_{OES} shell thickness (8 % r.a.). The remaining r.a. (14.9 %) corresponds to 6, 8 and 10-nm core diameter. The presence of these less-abundant Nps is necessary to achieve an optimum fit of experimental optical extinction spectrum in the long-wavelength

range. These hollow-metal structures have been observed by other authors using different fabrication techniques. For example, Desarkar et al. (2013) obtained Zn/ZnO hollow Nps by laser ablation in liquids, while Ben Moshe and Markovich (2011) and Selvakannan and Sastry (2005) produced colloidal hollow silver, gold, and platinum Nps by fast chemical reduction.

The distributions of core radii and shell thicknesses shown in the inset of Fig. 4 are in good agreement with experimental results previously obtained from TEM and AFM, which will be discussed below.

AFM analysis

AFM was used to characterize shape and size of single Nps and their 2*d* self-assembled fractal structures. The imaging of the colloids generated by ultrashort pulse laser ablation was performed over samples dried at 36 and 50 °C final temperatures. In the former case, for a dilution of 1/50 (v/v), we obtained AFM images showing isolated silver Nps or rosette-like structures. Figure 5a shows the image of a 7 μm × 7 μm scanned area where only small-sized isolated Nps are observed. Figure 5b shows the profiles of the Nps scanned by lines 1–5 in Fig. 5a. The obtained diameters are 9.4, 20.8, 9.2, 13, 7, and 4 nm, respectively.

Figure 6a shows the AFM image of a 5 μm × 5 μm scanned area where rosette-like structures can be observed. Clusters of closed rosette-like structures (average height 2 nm) that are limited by a plain region can be observed (lower and left sides of the Fig. 6).

To analyze the self-similarity property of these structures, we used box-counting method analysis (Li et al. 2009) which is a good approximation of Hausdorff dimension d_f (Feder 1988). This methodology, shown in Fig. 6b, was applied to the selected region of rosettes limited by dashed lines in Fig. 6a. The corresponding binary image used to calculate the fractal dimension is shown in the inset of Fig. 6b. The letters *b* and *n* represent the box size, in pixel units, in the horizontal axis and the number of boxes in the vertical axis, respectively. Full line corresponds to a linear regression fit of the data (dots). Dashed line shows the limit for a non-fractal dimension structure. The slope of the linear regression yields the fractal dimension $d_f = 1.70 \pm 0.02$.

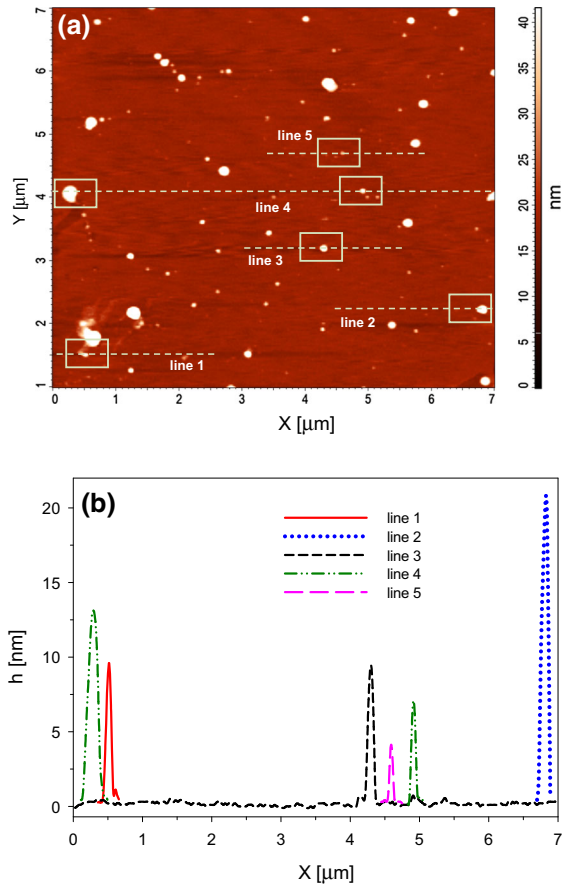

Fig. 5 **a** AFM image of 1/50 (v/v) Ag colloid dried at the 36 °C. **b** Height profiles along the *five dashed lines* in **a**. *Line 4* contains profiles of two Nps

When the Ag colloid at a dilution of 1/100 (v/v) was dried at 50 °C, silver fractal structures were observed in many areas of the sample. Figure 7a shows an example of this kind of structure in a 30 μm × 30 μm scanned area. Ramified structures in different development stages can be observed. Fractal aggregate size ranges between 5 and 14 μm and most of them are elongated in a preferred direction, indicated in the image by an arrow. This preferred orientation may be related to the crystalline anisotropy of the mica substrate which displays a trigonal symmetry. Small white dots correspond to isolated silver Nps which in some cases are decorating the fractal structures. An example of this last case is depicted in Fig. 7b, where the height profile corresponding to the scanned line labeled by a dashed line in Fig. 7a is shown. It can be seen that a sharp peak at about $X = 7$ μm, indicating

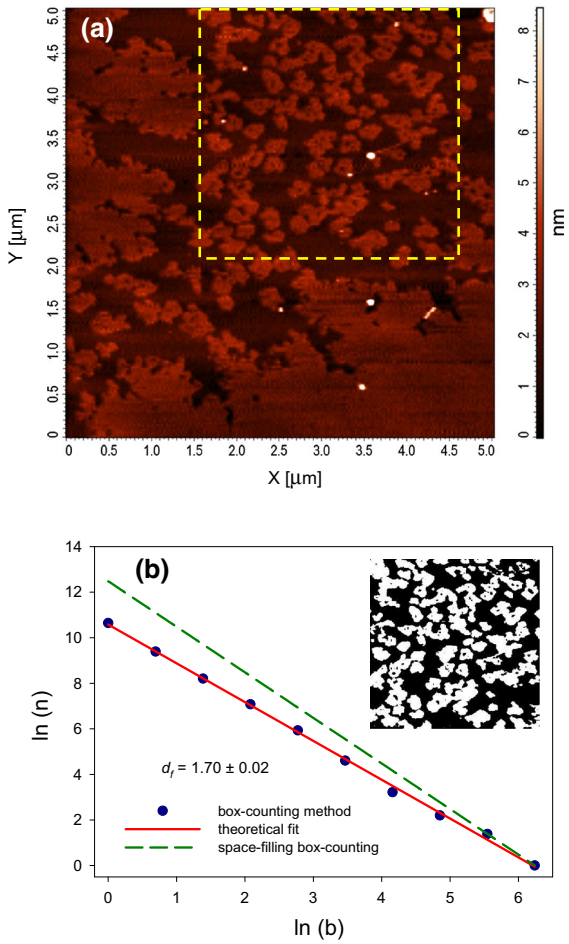

Fig. 6 **a** AFM image of rosette-shaped fractal structure limited by a plain region obtained from 1/50 (v/v) Ag colloid dried at 50 °C, and **b** double natural logarithm plot of number of boxes (n) versus box size (b, *filled dots*). Linear regression used to calculate fractal dimension (*full line*) compared with non-fractal dimension (*dashed line*). Binary image used to calculate fractal dimension is shown in the *inset*

the presence of a single Np of 10 nm size, is superimposed on the profile of a fractal-like structure. Inset shows the profile of fractal structure enclosed in the solid line rectangle in Fig. 7a. The average height of this ramified-like structure is about 2 nm. Figure 7c shows the corresponding binary image of Fig. 7a used to calculate its fractal dimension, yielding $d_f = 1.67 \pm 0.01$ as shown in Fig. 7d. Physical fractals like those shown in Fig. 7a differ from mathematical fractals in the fact that self-similarity holds only for finite length scales. Scaling relation holds from a minimum size of 30 nm to maximum cluster size of 14 µm. The minimum size is related to the image pixel size.

SAXS

The scattering differential cross section obtained by SAXS technique for the as-prepared silver aqueous colloid is shown in Fig. 8. As stated before, the main fractal properties are self-similarity and a scaling relation (power law form) for the increase of mass and number of particles with distance (Schaefer et al. 1984). SAXS yields a direct measurement of the mass fractal dimension under scaling arguments. Since we are dealing with physical fractals, the aggregate has a finite size (ξ), so self-similarity holds only for finite length scales and power law behavior occurs inside the aggregate, i.e., is limited by ξ and by primary particle finite size D'.

SAXS pattern in Fig. 8 can be well fitted with models involving the structure function $S(q)$. Scattering curve analysis was performed using the analytic form of $S(q)$ (Freltoft et al. 1986; Chen and Teixeira 1986):

$$S(q\xi,\ D') = 1 + \frac{d_f \Gamma(d_f - 1)}{(qD')^{d_f}} \frac{\sin[(d_f - 1)\tan^{-1}(q\xi)]}{(1 + 1/(q\xi)^2)^{\frac{d_f - 1}{2}}}. \quad (4)$$

The differential cross section against q, displayed in Fig. 8, was fitted with $\partial\Sigma/\partial\Omega = N_p(\Delta\eta V_p)^2 P(q) S(q\xi, D')$, where $P(q)$ is the spherical single-particle form factor weighted with a size log-normal distribution of median $\log(D')$ and standard deviation σ as described in (Fernández van Raap et al. 2012). Core–shell form factor is not used because this small shell size cannot be distinguished from size polydispersity effects. $\Gamma(d_f - 1)$ is the gamma function, d_f is the fractal dimension, and N_p, V_p, and $\Delta\eta$ are parameters related to the particle: number density, volume, and difference scattering length density, respectively. For the fitting, D' value was constrained to be equal to median value from TEM analysis of Fig. 1d and σ, ξ, $\Delta\eta$, and d_f were varied. Relevant fitted values are $\sigma = 0.344 \pm 0.002$, $\xi = (31 \pm 4)$ nm and $d_f = 2.48 \pm 0.02$. From $\langle D_{SAXS} \rangle = D' e^{\sigma^2/2}$, a mean particle size value of (5 ± 1) nm is obtained. Mean sizes derived from TEM, SAXS, and OES are in good agreement. SAXS pattern of the analyzed colloidal suspension is

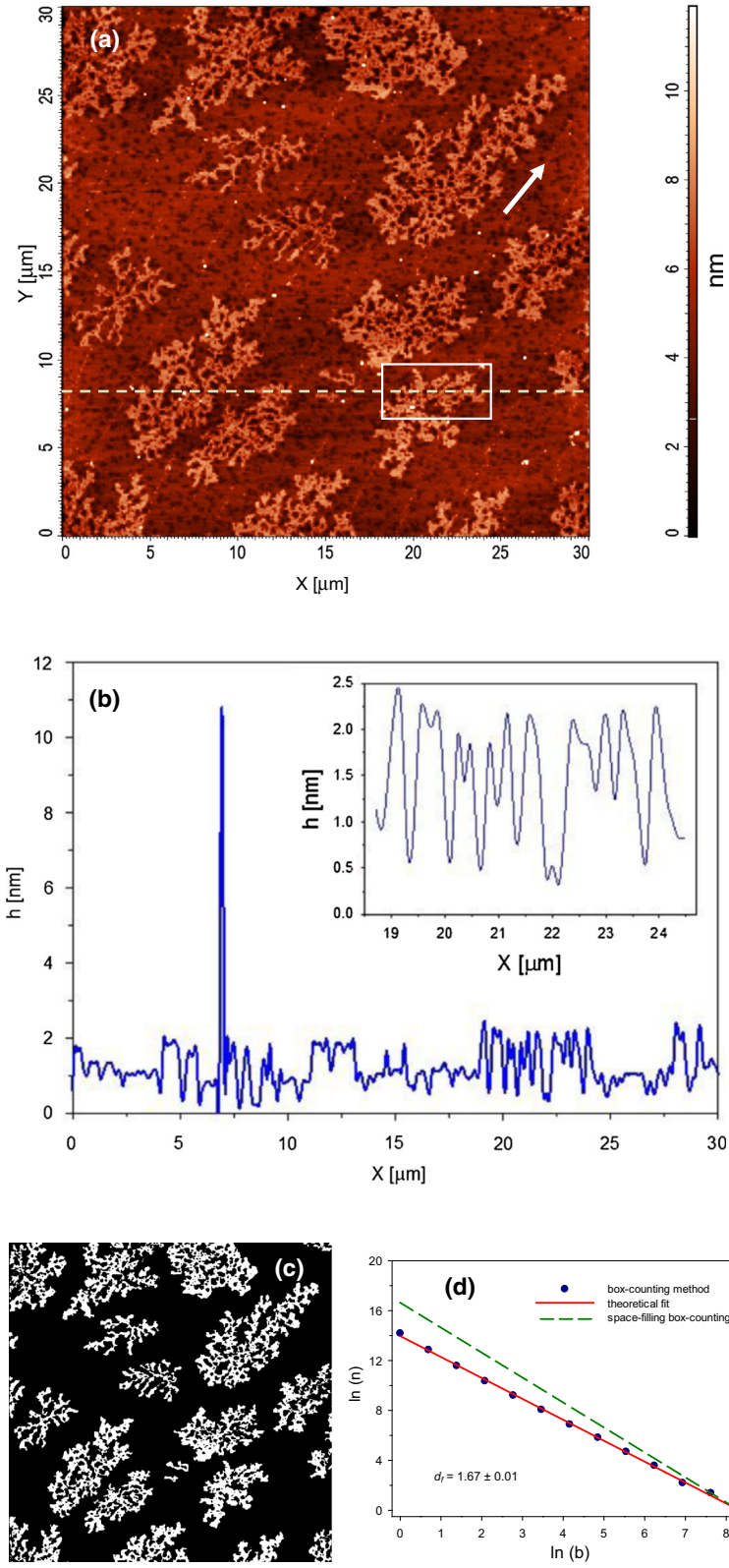

Fig. 7 **a** AFM image of novel silver fractal-like structure from 1/100 (v/v) Ag colloid dried at 50 °C. **b** Height profile along *dashed line* in **a**. *Inset* shows an enlarged plot of the fractal height profile enclosed in the *solid line rectangle*. **c** Binary image used to calculate fractal dimension using box-counting method. **d** Double logarithmic plot of number of boxes *n* versus box size *b* (*filled dots*). Linear regression used to calculate the fractal dimension (*full line*) compared with non-fractal dimension (*dashed line*)

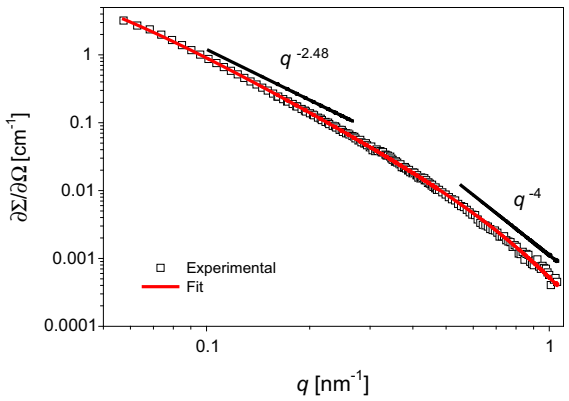

Fig. 8 Double-logarithmic representation of Ag colloidal suspensions SAXS data expressed as differential cross section $\partial\Sigma/\partial\Omega$ against momentum transfer vector q. The *full line* stands for the best fit obtained with a fractal model of aggregation as described in the text

consistent with Nps forming fractal structures of 31 nm size and fractal dimension $d_f = 2.5$.

Discussion

In recent years, several papers dealing with the fractal character of both metal and dielectric nanostructures generated after pulsed laser ablation in liquids have been published. These works encompass a variety of pulsed laser regimes and energies, environments, type of base material, and various substrates resulting in quite different fractal structures. For instance, Yan et al. (2013) using high-purity Ag target in water, as in our work, but different laser (a KrF excimer laser, $\lambda = 248$ nm, 30 ns pulse width) generated Ag–Ag_2O complex nanostructures. They obtained Ag_2O non-spherical (nanorice and flower-like) structures when a drop of the colloidal sample was evaporated on a Si surface. The different rice-shaped particles as well as the ensembles obtained are caused by the coalescence of clusters at the rim of the drop due to the radial flow that appears inside an evaporating drop. On the other hand, Cavaliere et al. (2013) used an fs laser ($\lambda = 800$ nm, 120 fs pulse width) for PLD of TiO_2 over Si wafers forming fractal TiO_2 nanostructures. Although the laser system is very similar to ours, the shape, morphology, and electronic band structure of the primary Nps are different. The aggregates deposited on the Si surface have a dendrite-like shape and its complexity depends on sample-target distance and laser fluence. Their fractal dimension d_f varies between 1.6 and 1.7 for fluences in the range 6.5–9.5 J/cm^2.

Colloidal suspensions obtained by fs laser ablation of an Ag solid target in water during our experiments are formed by different nanometric structures. When drops diluted at 1/50 (v/v) were dried at 9 °C initial temperature difference, isolated single Nps or Nps decorated rosette-like structures with $d_f = 1.70 \pm 0.02$ were observed. On the other hand, when drops diluted at 1/100 (v/v) were dried at 25 °C initial temperature difference, well-ramified (dendritic) structures with $d_f = 1.67 \pm 0.01$ were found. These Hausdorff dimension values indicate that these structures are fractal and are due to aggregation governed by random processes.

If the random process proceeds via the attaching of new particles to the boundary of a previously existing seed, then the cluster will have a more or less spherical shape (Eden clusters $d_f = 1.70$). This is the case of our rosette-like structures mentioned previously. However, if the aggregation proceeds via a diffusion-like random walk process, then the cluster will end up with a ramified structure characterized by a fractal dimension $d_f = 1.67$ or with a more thick branch-ramified structure (modified DLA or MDLA characterized with $d_f = 1.67$; Tokuyama and Kawasaki 1984). This is the case of our dendritic-like structures.

It is generally accepted that the fabrication process of Nps arising from fs pulse laser ablation of a metal sample immersed in a liquid starts in the high-temperature high-pressure plasma generated at the solid–liquid interface (Yan and Chrisey 2012). Our experiments were carried out at high laser fluence (450 J/cm^2), so just after ablation the ejected particles had very high kinetic energy with a reduced probability of aggregation. Adiabatic expansion is followed by a rapid cooling of the plasma plume thus enhancing cluster formation. Wagener et al. (2013) used in situ time-resolved SAXS of nanosecond laser ablation in liquid to study the dynamics of silver Np formation. They concluded that after laser ablation, a vapor-filled cavitation bubble containing two individual species identified as compact primary particles of 8–10 nm size and larger agglomerates of 40–60 nm size were formed. For this nanosecond laser, the bubble collapsed after 220 μs.

In our low-concentrated colloidal suspension, when the Nps thermalize and their kinetic energy reduce to the thermal kinetic energy, they aggregate forming fractal structure through DLA mechanism, as it is inferred from SAXS analysis. A direct measurement of the mass fractal dimension in the as-prepared suspension indicated the presence of nanometric fractal clusters with $d_f = 2.48 \pm 0.02$.

In the case of $2d$ fractal structures, the resulting structure depends on the colloid concentration and on the initial temperature gradient of the drying process indicating that the fractals are formed during drop drying and that Nps diffusion inside the drop contributes to the formation of the observed $2d$ fractal structures. In this process, the deposited drop undergoes evaporation at fast temperature rise inducing nonequilibrium conditions.

The nature of fractal growth governed by diffusion is similar in $2d$ and $3d$, but displaying distinctive fractal dimension depending on the Euclidean space dimension (d). Tokuyama and Kawasaki (1984) brought forward a calculating formula for fractal dimension d_f based on d as $d_f = (d^2 + 1)/(d + 1)$ valid for DLA growth. The fractal dimension derived from the analysis of SAXS results is in agreement with the value of $d_f = 2.5$ derived with this equation when $d = 3$. On the other hand, fractal dimension determined using the box-counting method on $2d$ AFM images of the sample diluted to 1/100 (v/v) and dried at 25 °C initial temperature difference result in $d_f = 1.67$ in agreement with this equation when $d = 2$. Summarizing, the DLA process governs the pattern of fractal structure in both $2d$ and $3d$ dimension growths.

Conclusions

We have shown for the first time the generation of self-assembled fractal Ag structures after pulsed fs laser ablation of a solid Ag target in water. By using two independent techniques (OES and TEM), we concluded that the original colloidal suspension is composed of very small isolated spherical Nps (4–5 nm size) and fractal aggregated particles. The isolated Nps have bare core and core–shell structures of the type Ag bare core, Ag–Ag_2O, and air–Ag, respectively, Ag–Ag_2O being the most frequent type (69 % r.a.).

The fractal structuring was in situ observed in the as-prepared suspension as $3d$ fractal aggregates of mean size 31 nm with fractal dimension $d_f = 2.5$. Ex situ imaging was obtained after evaporation of a drop of diluted colloidal suspension on a mica substrate using different drying rates. Distinct $2d$ structures were observed, going from isolated single Nps or rosette-like structure ($d_f = 1.7$) to well-ramified clusters of 14 μm in-plane length ($d_f = 1.67$) for increasing dilution and drying rate. The observed $3d$ fractal structures are formed after thermalization of the colloidal suspension, while $2d$ fractals are formed during drop drying limited by a surface. The $2d$ ramified and $3d$ self-assembled fractals are consistent with DLA model.

Acknowledgments This work was Granted by PIP 0394 and PIP 0111 of CONICET, PME2006-00018 and PICT 00898 of ANPCyT, and 11/I151 (Facultad de Ingeniería), 11/x556 (Facultad de Ciencias Exactas) of Universidad Nacional de La Plata, Argentina. We thank C2NANO-Brazilian Nanotechnology National Laboratory (LNNano) and Brazilian Synchrotron Light Laboratory (LNLS) at Centro Nacional de Pesquisa em Energia e Materiais (CNPEM)/MCT (#14825 and 14827) for the use of TEM and the use of D01B-SAXS2 beam line for data acquisition under Proposal #13714. AFM was carried out at LFAyM of Instituto de Física La Plata (IFLP-CONICET). D. C. Schinca is Member of Comisión de Investigaciones Científicas de la Provincia de Buenos Aires (CIC). L. B. Scaffardi, M. B. Fernández van Raap, and P. Mendoza Zélis are researchers of CONICET, J. M. J. Santillán is a postdoc fellow of CONICET, Argentina and D. Coral is Fellow of COLCIENCIAS, Colombia and Doctoral student of UNLP.

References

Baker SH, Thornton SC, Edmonds KW, Maher MJ, Norris C, Binns C (2000) The construction of a gas aggregation source for the preparation of size-selected nanoscale transition metal clusters. Rev Sci Instrum 71(8):3178–3183

Barcikowski S, Hahn A, Kabashin AV, Chichkov BN (2007) Properties of nanoparticles generated during femtosecond laser machining in air and water. Appl Phys A 87(1):47–55

Ben Moshe A, Markovich G (2011) Synthesis of single crystal hollow silver nanoparticles in a fast reaction-diffusion process. Chem Mater 23(5):1239–1245

Bewig L, Buck U, Mehlmann Ch, Winter M (1992) Seeded supersonic alkali cluster beam source with refilling system. Rev Sci Instrum 63(8):3936–3938

Bohren CF, Huffman DR (1998) Absorption and scattering of light by small particles. Wiley, New York

Cavaliere E, Ferrini G, Pingue P, Gavioli L (2013) Fractal TiO_2 nanostructures by nonthermal laser ablation ambient pressure. J Phys Chem C 117(44):23305–23312

Chen S-H, Teixeira J (1986) Structure and fractal dimension of protein–detergent complexes. Phys Rev Lett 57(20): 2583–2586

Desarkar HS, Kumbhakar P, Mitra AK (2013) One-step synthesis of Zn/ZnO hollow nanoparticles by the laser ablation in liquid technique. Laser Phys Lett 10(5):055903–055908

Ding H-P, Xin G-Q, Chen K-C, Zhang M, Liu Q, Hao J, Liu H-G (2010) Silver dendritic nanostructures formed at the solid/liquid interface via electroless deposition. Colloids Surf A 353(2–3):166–171

Dong J, Gong J, Liu J, Chen M, Yan X (2012) The decoration of silver fractal-like nanostructure with Ag nanoparticles on the plastic slide for surface enhanced fluorescence. Electrochim Acta 60:264–268

Feder J (1988) Fractals. Plenum Press, New York

Fernández van Raap MB, Mendoza Zélis P, Coral DF, Torres TE, Marquina C, Goya GF, Sánchez FH (2012) Self organization in oleic acid-coated $CoFe_2O_4$ colloids: a SAXS study. J Nanopart Res 14:1072

Freltoft T, Kjems JK, Sinha SK (1986) Power-law correlations and finite-size effects in silica particle aggregates studied by small-angle neutron scattering. Phys Rev B 33(1): 269–275

Hou SM, Ouyang M, Chen HF, Liu WM, Xue ZQ, Wu QD, Zhang HX, Gao HJ, Pang SJ (1998) Fractal structure in the silver oxide thin film. Thin Solid Films 315(1–2):322–326

Ishii K, Amano K, Hamakake H (1999) Hollow cathode sputtering cluster source for low energy deposition: deposition of Fe small clusters. J Vac Sci Technol A 17(1):310–313

Johnson PB, Christy RW (1972) Optical constants of the noble metals. Phys Rev B 6:4370–4379

Kabashin AV, Meunier M (2006) Laser ablation based synthesis of nanomaterials. In: Perrière J, Millon E, Fogarassy E (eds) Recent advances in laser processing of materials. Elsevier, Oxford, pp 1–36

Kittel C (2007) Introduction to solid state physics. Wiley, New York

Kreibig U, Vollmer M (1995) Optical properties of metal clusters. Springer, Berlin

Li J, Du Q, Sun C (2009) An improved box-counting method for image fractal dimension estimation. Pattern Recognit 42(11):2460–2469

Liu B, Wang M (2013) Electrodeposition of dendritic silver nanostructures and their application as hydrogen peroxide sensor. Int J Electrochem Sci 8(6):8572–8578

Parfenov A, Gryczynski I, Malicka J, Geddes CD, Lakowicz JR (2003) Enhanced fluorescence from fluorophores on fractal silver surfaces. J Phys Chem B 107(34):8829–8833

Qiu JH, Zhou P, Gao XY, Yu JN, Wang SY, Li J, Zheng YX, Yang YM, Song QH, Chen LY (2005) Ellipsometric study of the optical properties of silver oxide prepared by reactive magnetron sputtering. J Korean Phys Soc 46:S269–S275

Qiu R, Zhang XL, Qiao R, Li Y, Kim YI, Kang YS (2007) CuNi dendritic material: synthesis, mechanism discussion, and application as glucose sensor. Chem Mater 19(17): 4174–4180

Qiu R, Cha HG, Noh HB, Shim YB, Zhang XL, Qiao R, Zhang D, Kim YI, Pal U, Kang YS (2009) Preparation of dendritic copper nanostructures and their characterization for electroreduction. J Phys Chem C 113(36): 15891–15896

Qu L, Dai L (2005) Novel silver nanostructures from silver mirror reaction on reactive substrates. J Phys Chem B 109(29):13985–13990

Santillán JM (2013) Estudio de propiedades ópticas de materiales nanoestructurados. PhD Thesis, Facultad de Ciencias Exactas, Universidad Nacional de La Plata (UNLP), Argentina. http://www.hd.lhandle.net/10915/30746

Santillán JMJ, Videla FA, Fernández van Raap MB, Schinca DC, Scaffardi LB (2012) Size dependent Cu dielectric function for plasmon spectroscopy: characterization of colloidal suspensions generated by fs laser ablation. J Appl Phys 112(5):054319

Santillán JMJ, Videla FA, Fernández van Raap MB, Muraca D, Scaffardi LB, Schinca DC (2013a) Influence of size-corrected bound-electron contribution on nanometric silver dielectric function Sizing through optical extinction spectroscopy. J Phys D 46(43):435301

Santillán JMJ, Videla FA, Fernández van Raap MB, Schinca DC, Scaffardi LB (2013b) Analysis of the structure, configuration and sizing of Cu and Cu oxide nanoparticles generated by fs laser ablation of solid target in liquids. J Appl Phys 113(13):134305

Scaffardi LB, Schinca DC, Lester M, Videla FA, Santillán JMJ, Abraham Ekeroth RM (2013c) Size-dependent optical properties of metallic nanostructures. In: Challa SSR (ed) Kumar UV–vis and photoluminescence spectroscopy for nanomaterials characterization. Springer, Heidelberg, pp 179–229

Schaefer DW, Martin JE, Wiltzius P, Cannell DS (1984) Fractal geometry of colloidal aggregates. Phys Rev Lett 52(26): 2371–2374

Schultz S, Smith DR, Mock JJ, Schultz DA (2000) Single-target molecule detection with nonbleaching multicolor optical immunolabels. Proc Natl Acad Sci USA 97(3):996–1001

Selvakannan PR, Sastry M (2005) Hollow gold and platinum nanoparticles by a transmetallation reaction in an organic solution. Chem Commun 13:1684–1686

Shelke PB, Nguyen VD, Limaye AV, Schall P (2013) Controlling colloidal morphologies by critical Casimir forces. Adv Mater 25(10):1499–1503

Siekmann HR, Lüder Ch, Faehrmann J, Lutz HO, Meiwes-Broer KH (1991) The pulsed arc cluster ion source (PACIS). Z Phys D 20:417–420

Singh M, Sinha I, Singh AK, Mandal RK (2011) Formation of fractal aggregates during green synthesis of silver nanoparticles. J Nanopart Res 13:69–76

Sun X, Hagner M (2007) Novel preparation of snowflake-like dendritic nanostructures of Ag or Au at room temperature via a wet-chemical route. Langmuir 23(18):9147–9150

Tokuyama M, Kawasaki K (1984) Fractal dimensions for diffusion-limited aggregation. Phys Lett A 100(7):337–340

Wagener P, Ibrahimkutty S, Menzel A, Plech A, Barcikowski S (2013) Dynamics of silver nanoparticle formation and agglomeration inside the cavitation bubble after pulsed laser ablation in liquid. Phys Chem Chem Phys 15(9):3068–3074

Wang Y, Camargo PHC, Skrabalak SE, Gu H, Xia YA (2008) Facile, water-based synthesis of highly branched nanostructures of silver. Langmuir 24(20):12042–12046

Wen X, Xie YT, Mak MWC, Cheung KY, Li XY, Renneberg R, Yang S (2006) Dendritic nanostructures of silver: facile synthesis, structural characterizations, and sensing applications. Langmuir 22(10):4836–4842

Yan Z, Chrisey DB (2012) Pulsed laser ablation in liquid for micro-/nanostructure generation. J Photochem Photobiol C 13(3):204–223

Yan Z, Bao R, Chrisey DB (2013) Generation of Ag–Ag_2O complex nanostructures by excimer laser ablation of Ag in water. Phys Chem Chem Phys 15(9):3052–3056

Zenkevich AV, Pushkin MA, Tronin VN, Troyan VI, Nevolin VN, Maximov GA, Filatov DO, Lægsgaard E (2002) Formation of Au fractal nanoclusters during pulsed laser deposition on highly oriented pyrolitic graphite. Phys Rev B 65:073406

Zhou Y, Yu SH, Wang CY, Li XG, Zhu YR, Chen ZY (1999) A novel ultraviolet irradiation photoreduction technique for the preparation of single-crystal Ag nanorods and Ag dendrites. Adv Mater 11(10):850–852